Colloidal Tin–Germanium Nanorods and Their Li-Ion Storage Properties

Maryna I. Bodnarchuk,[†,‡,§,*] Kostiantyn V. Kravchyk,[†,‡,§] Frank Krumeich,[†] Shutao Wang,[†,‡] and Maksym V. Kovalenko[†,‡,*]

[†]Institute of Inorganic Chemistry, Department of Chemistry and Applied Biosciences, ETH Zürich, CH-8093 Zürich, Switzerland, and [‡]Laboratory for Thin Films and Photovoltaics, Empa-Swiss Federal Laboratories for Materials Science and Technology, CH-8600 Dübendorf, Switzerland. [§]These authors contributed equally to this work.

ABSTRACT We report a facile colloidal synthesis of tin–germanium (Sn–Ge) heterostructures in the form of nanorods with a small aspect ratio of 1.5–3 and a length smaller than 50 nm. In the two-step synthesis, presynthesized Sn nanoparticles act as a low-melting-point catalyst for decomposing the Ge precursor, bis-[bis(trimethylsilyl)amido]Ge(II), and for crystallization of Ge *via* solution–liquid–solid growth mechanism. Creation of such Sn–Ge nanoheterodimers can serve as a well-controlled method of mixing these nearly immiscible chemical elements for the purpose of obtaining Sn–Ge nanocomposite electrodes for high-energy density Li-ion batteries. Comparable mass content of Sn and Ge leads to synergistic effects in electrochemical performance: high charge storage capacity above 1000 mAh g^{-1} at a relatively high current density of 1 A g^{-1} is due to high theoretical capacity of Ge, while high rate capability is presumably caused by the enhancement of electronic transport by metallic Sn. At a current density of 4 A g^{-1}, Sn–Ge nanocomposite electrodes retain up to 80% of the capacity obtained at a lower current density of 0.2 A g^{-1}. Temporally separated lithiation of both elements, Sn and Ge, at different electrochemical potentials is proposed as a main factor for the overall improvement of the cycling stability.

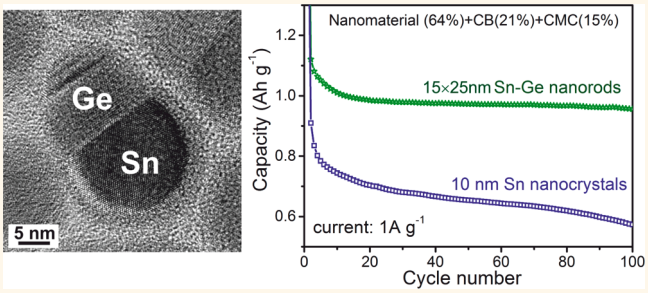

KEYWORDS: nanocrystals · nanorods · synthesis · heterostructures · Li-ion batteries · energy storage

Owing to their excellent size, shape, and compositional homogeneity, colloidally synthesized inorganic nanostructures are considered as future building blocks for novel electronic and optoelectronic materials.[1] At present, monodisperse inorganic nanocrystals (NCs) smaller than 20 nm and with size distributions not exceeding 10–20% serve as a convenient platform for studying individual size-dependent properties of NCs (luminescent quantum dots, nanomagnets, and catalysts)[2–4] and collective optical or electronic responses in NC arrays (charge transport, lasing, photoconductivity, photovoltaics).[5–8] There is also a growing recognition that complex electron and ion transport phenomena occurring in Li-ion batteries (LiBs) and in related electrochemical energy storage technologies can also be better understood and further tailored using well-defined NCs as active electrode materials.[9–15] In the last 10 years, nanostructuring has revived a tremendous interest to a large number of those alternative cathode and anode materials which, despite the ability to uptake large quantities of Li-ions, were previously discarded on the basis of poor electronic conductivity, slow reaction kinetics, or large volumetric changes. Nonexhaustive list of these substances includes group IV elements (Si, Ge, Sn), their alloys and heterostructures, as well as metal oxides and fluorides.[16–20]

From the perspective of Li-ion storage efficiency, through the creation of Sn–Ge nanoheterostructures, potentially the best of both elements can be realized. Metallic Sn can enhance an electronic transport, while Ge can boost the overall capacity to at least 1000 mAh g^{-1}. Sn and Ge have much higher theoretical gravimetric charge storage capacities than commercially used graphite (373 mAh g^{-1} for LiC_6): 990 mAh g^{-1} for Sn ($Li_{22}Sn_5$) and 1624 mAh g^{-1} for Ge ($Li_{22}Ge_5$).[16] We note that the theoretical capacity for Ge at ambient conditions is still debated, with the most conservative estimate being 1384 mAh g^{-1}, corresponding to $Li_{15}Ge_4$.[21] We should also mention that

* Address correspondence to bodnarchuk@inorg.chem.ethz.ch, mvkovalenko@ethz.ch.

Received for review November 10, 2013 and accepted February 1, 2014.

Published online February 01, 2014
10.1021/nn4058227

even higher capacities are theoretically achievable for silicon anodes (3579 mAh g^{-1} for $Li_{15}Si_4$). Rate capability, which is the ability to retain the capacity with increasing current density, is also an important consideration. Li-ion mobility and electronic conductivity within the active material often limit the capacity at high current densities. Room-temperature Li-ionic mobilities were reported to be 400 and 6000 times higher in Ge than in Si and Sn, respectively.[22] Furthermore, Ge and especially metallic Sn possess much higher electrical conductivities than Si, by at least factor of 10^4 for Ge. To this end, nanoparticulate Ge was recently shown to support high-rate performance, with capacities of 700 mAh g^{-1} through 500 cycles at 10C charge/discharge rates.[10] The major drawback of all group IV elements is the drastic volume expansion by up to 230% for Ge and 260% for Sn upon full lithiation. Not a surprise is the fact that substantial cycling stabilities for group-IV-based anode materials have been achieved only for nanostructured electrodes, including both one-dimensional nanowires and nearly isotropic nanoparticles.[10,23−28]

This study was motivated by (i) the considerable lack of preparative methods for high-quality group IV colloidal nanostructures (Sn, Ge, Si, and combinations thereof)[1] and (ii) well-recognized potential of such nanostructures as high-energy density anode materials in Li-ion batteries.[10,23−26,28] We demonstrate that monodisperse Sn nanoparticles (NPs),[29] with the bulk melting point of 232 °C, can act as liquid catalysts for the solution−liquid−solid (SLS) growth of highly crystalline Ge at temperatures as low as 250 °C in high-boiling organic solvents. As a result, highly uniform colloidal Sn−Ge nanorod (NR) heterostructures can be produced (Scheme 1, Figure 1, and Figure S1 of the Supporting Information). In a one-pot strategy, we used bis[bis(trimethylsilyl)amido]germanium(II), $Ge[N(SiMe_3)_2]_2$, as a convenient and reactive precursor that can be added directly into the crude solution of Sn NPs. Furthermore, we show that Sn−Ge NRs exhibit superior Li-ion storage properties as compared to elemental Sn and Ge counterparts. In particular, colloidal Sn−Ge NRs exhibit stable cycling with charge storage capacities above 1000 mAh g^{-1}, close to the value expected theoretically. Although there has been a growing interest in Sn−Ge composites for Li-ion batteries,[10,30,31] this work shows a first example of well-defined colloidal Sn−Ge NCs. Because Sn and Ge are nearly immiscible on atomic scale, such NCs represent an ultimately most homogeneous mixture of these two elements, which can hardly be obtained *via* mechanical mixing such as ball-milling.

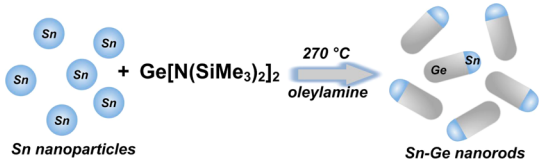

Scheme 1. Outline of the one-pot, solution−liquid−solid growth of colloidal Sn−Ge nanorods using presynthesized Sn nanoparticles as catalyst.

Solution−Liquid−Solid Growth of Sn−Ge Nanorods. Catalyzed growth of NRs and nanowires implies the use of a liquid metal nanodroplet as a catalyst which forms eutectic mixture with the target NR material. Oversaturation of the catalyst droplet above the eutectic solubility leads to the reduced activation barrier for precipitation, crystallization, and growth. Typical examples of such eutectics are Au−Si (19% Si, T_m = 363 °C) and Au−Ge (28.5% Ge, T_m = 358 °C).[32] These high solubilities indicate that energetic costs of dissolving Ge or Si in Au are low, and consequently, the cost of having supersaturation is also relatively low, leading to eutectic temperatures well below the melting point of each element. The low melting point of the eutectic mixture allows carrying out such growth at low temperatures in organic solvents, where the metallic catalyst is dispersed in the form of colloidal nanoparticles. Such colloidal approach has been named solution−liquid−solid growth (SLS growth),[33−35] in order to highlight similarities and differences with more conventional vapor−liquid−solid growth (VLS growth). The colloidal synthesis offers many benefits, of which most important is the precise control over the size, shape, and composition, as well as tailorable surface

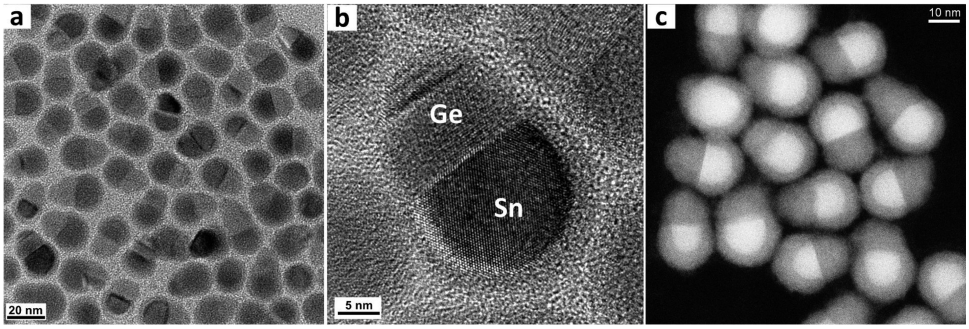

Figure 1. (a) Low-resolution and (b) high-resolution transmission electron microscopy (TEM) images, and (c) high-angle annular dark field scanning transmission electron microscopy (HAADF-STEM) image of Sn−Ge nanorods.

chemistry and convenient handling of colloidal solutions.[34] Sn is potentially an interesting catalyst for growing Si and Ge. As a group IV element, it is an isoelectric and rather neutral electronic impurity. Contrary to Au-based eutectics, much lower eutectic solubilities of Si or Ge in Sn were reported in bulk phase diagrams: below 0.5% for Ge (Figure S2) and $\leq 10^{-4}$ atom % for Si,[36] leading to the eutectic point close to the melting point of pure Sn (232 °C). Despite these low solubilities, liquid-phase Sn-catalyzed growth of Si nanorods[37] and nanowires[26] has been recently reported. Additionally, bismuth NPs have been shown to efficiently catalyze the growth of colloidal Ge NRs,[38] despite the comparably low solubility of Ge in Bi (below 1%). These reports indicate that high solubility at the eutectic point is not a key requirement for the catalytic growth, and the reduced solubility may in fact also play a beneficial role when a controlled synthesis of low aspect ratio NRs is targeted. From the perspective of Li-ion batteries, our goal was indeed to obtain such short NRs with comparable volumetric fractions of Sn and Ge.

To take advantage of such low-melting-point catalyst as Sn, one should find a suitable Ge precursor with high reactivity at temperatures not much higher that the melting point of the catalyst in order to prevent the growth and aggregation of catalyst droplets. In the footstep of the recent reports on the use of alkyl- and silylamides of metal and metalloids for precision synthesis of colloidal nanomaterials,[7,8,16,29,39,40] we find that analogous compound, $Ge[N(SiMe_3)_2]_2$, shows suitable reaction kinetics when combined with colloidal Sn NPs in oleylamine (OLA) as a coordinating solvent at temperatures as low as 250−300 °C. Figure 1 shows highly crystalline Sn−Ge nanorods, on average 25 nm long and 15 nm wide, obtained just 2−3 min after the injection of Ge precursor mixed with monodisperse 15 nm Sn NPs into hot OLA at 300 °C (temperature drops to 255−265 °C after injection). Alternatively, a one-pot synthesis can be realized by adding Ge precursor directly into a crude solution of Sn NPs at 230 °C, followed by the heating to 250−270 °C.

Similarly to other highly covalent semiconductor materials (III−V compounds, silicon), colloidal synthesis of crystalline Ge NCs has always been a formidable challenge. Our analysis of literature and a recent review by Vaughn and Schaak[41] show that simultaneous size control and crystallization of Ge has been especially problematic at temperatures below 300 °C. So far, the most successful approaches to crystalline and monodisperse colloidal Ge NPs were based on the reduction of Ge halide precursors in alkylamine as a solvent with the reaction times of one to several hours.[39,42,43] The use of presynthesized $Ge[N(SiMe_3)_2]_2$ as a precursor for Ge NPs, without addition of catalyst particles, has been already reported,[44] showing rather modest control

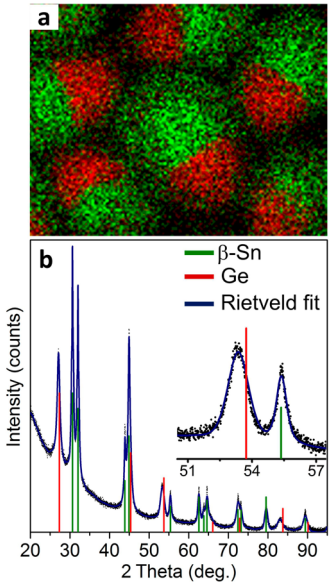

Figure 2. (a) Elemental EDX-STEM maps for Sn−Ge nanorods (same as shown in Figure 1): Ge (red, L-line) and Sn (green, L-line). (b) Powder XRD pattern of Sn−Ge NRs. Inset shows the shift of Ge reflections (increase of the lattice constant) due to alloying with Sn.

over the size distribution and uniformity. Our reference experiment conducted without Sn NPs also yielded poorly crystalline, nonuniform Ge NPs in 5−15 nm range of sizes (Figure S3). Similarly to our findings, during the preparation of this article, Read *et al.* have reported the synthesis of highly crystalline Au−Ge heterodimers by decomposing $Ge[N(SiMe_3)_2]_2$ in the presence of Au NCs as seeds.[45]

The heterodimeric structure with a flat Sn−Ge interface is apparent from the pronounced Z-contrast in TEM and STEM images (Figure 1), as well as from EDX-STEM (energy-dispersive X-ray spectrometry acquired in STEM mode) elemental maps (Figure 2a) and from EDX spot analysis (Figure S4). Powder XRD patterns (Figure 2b) and electron diffraction patterns (Figure S5) can be indexed to tetragonal β-Sn and diamond cubic Ge. Ge side of the Sn−Ge NR grows in the ⟨111⟩ crystallographic direction, corresponding to (111) plane at the Sn−Ge interface. The high-resolution TEM survey of 30 nanorods shows that many contain (111) twin planes or are kinked when they are longer (Figure S6). Powder XRD patterns (Figure 2) clearly reveal that while the reflections from the Sn part of Sn−Ge heterostructure perfectly match the lattice parameters of β-Sn (space group *I*41/*amd*, JCPDS 00-04-0673), the lattice constant for Ge, estimated by Rietveld refinement (difference plot and refinement parameters are shown in Figure S7), has increased to 5.694 Å, that is, by 0.65% with respect to the bulk lattice constant of Ge (5.568 Å, space group *Fd*3*m*, JCPDS 00-004-0545). Assuming alloying of Ge with Sn, extrapolation toward bulk lattice constant of 6.491 Å for cubic diamond Sn (α-Sn)[46] provides that ∼4.3% of Sn is

incorporated into Ge side of the Sn−Ge dimer (Vegard's law). Although the bulk phase diagram indicates that the solubility of Sn in Ge does not exceed 1% at 200−300 °C, higher Sn concentrations up to 10% were indeed experimentally demonstrated for rather nonequilibrium crystalline Sn−Ge heterostructures,[36] such as rapidly cooled melts[47] or nanopowders synthesized by laser photolysis in a gas phase.[30] Raman spectra of Sn−Ge nanorods (Figure S8) provide further evidence for the incorporation of Sn into Ge: a clear shift of Ge Raman peak from 295 to 292 cm^{-1} is observed. Such shift is consistent with $\Delta\omega \sim 6$ cm^{-1} in $Ge_{0.923}Sn_{0.077}$ thin films[48] and is closer to theoretical predictions for relaxed $Ge_{1-x}Sn_x$ [$\Delta\omega(x) = -95.1x$ cm^{-1}] rather than for strained material [$\Delta\omega(x) = -31.1x$ cm^{-1}].[49]

The width and the lengths of Sn−Ge NRs can be adjusted by both the size of the Sn seeds and by the overall molar ratio between Ge and Sn in the system. Starting with 15 nm Sn NPs as seeds, 25 nm long rods are obtained at Ge/Sn molar ratios of 10, while longer but kinked 40−50 nm Sn−Ge NRs are grown at Ge/Sn = 25 (Figure S9). Further increase of Ge concentration leads to a separate nucleation of polydisperse Ge NPs. The smallest Sn−Ge heterodimers are obtained using 10 nm Sn seeds and lower growth temperatures of 250 °C (Figure S10). At higher temperatures of 310−340 °C, Sn NP seeds uncontrollably aggregate and the fast reaction kinetics leads to nonuniform nanowires (Figure S11). Due to their higher homogeneity and comparable and reproducible Sn and Ge volume fractions, only 15 × 25 nm Sn−Ge NRs were selected for studying their Li-ion storage properties.

Li-Ion Storage Properties of Sn−Ge Nanorods. For simplicity, we denote the weight fraction of an active electrode material as *f*, being in the range of 0−1 (*e.g.*, 0−100 wt %). So far, the most common approach to achieve improved cycling stability for nanoparticulate alloy-based anodes is to mix an active material (f_{AM} = 0.3−0.8) with large amounts of amorphous carbon as a conductive additive/matrix (f_{CB} = 0.1−0.6) and water-soluble polymeric binder such as carboxymethylcellulose (CMC, used this study, *f* = 0.1−0.25).[10,29,50−54] The advent of CMC binder, as well as other sugarlike moieties such as naturally derived sodium alginate, has dramatically improved the reported performance characteristics of Si-, Ge-, and Sn-based anodes in the recent years.[28,29,40,53,54] Carbon black (CB) is a common conductive additive. At low mass fractions of an active material (f_{AM} = 0.2−0.4), individual particles or their small aggregates can be assumed to be well-separated and capacities close to theoretical are often achieved. Higher fractions of an active material (f_{AM} = 0.6−0.8) provide more practical overall charge storage capacities of the electrode film (C^{film}) but often at the expense of reduced cyclability due to mechanical instabilities caused by volumetric changes during insertion and extraction of Li-ions. In the following, we will report three kinds of charge storage capacities. First is the overall capacity (C^{film}), which is a direct output of the measurement, obtained by dividing the total stored charge by the total mass of the electrode (active material + binder + carbon). Commonly reported in literature, however, is the highest estimate for the storage capacity of an active material, denoted here as C^{max}, obtained by normalizing C^{film} to the mass fraction of an active material, neglecting the capacity of the conductive additive:

$$C^{max} = C^{film}/f_{AM} \quad (1)$$

Strictly speaking, for CB as a conductive additive, this practice is correct only for cathode materials but not for anodes with high volume fractions of CB, cycled in the voltage ranges down to 0 V *vs* Li^+/Li. We therefore also introduce the most conservative estimate for the storage capacity of an active material (C^{min}), by taking into account the capacity of CB (C_{CB}):

$$C^{min} = C^{max} - C_{CB}\frac{f_{CB}}{f_{AM}} \quad (2)$$

We find that electrodes made of pure CB with 15% of CMC as a binder, cycled under identical conditions with charge/discharge currents of 1000 mA g^{-1} and 0.005−2 V voltage window, yield C_{CB} = 200 mAh g^{-1}. In this study, Sn/Ge NRs were tested in coin-type Li-ion battery cells by cycling against metallic Li between 0.005 and 2.0 V *vs* Li/Li^+ at various *C* rates (1*C* = 1000 mA g^{-1}). The samples were solution-casted films with the mass loading of ∼0.5 mg cm^{-2}. For improved long-term cycling stability, fluoroethylenecarbonate (FEC) additive, which improves the stability of the solid-electrolyte interface (SEI),[40] was added to the standard electrolyte (1 M $LiPF_6$ in 1:1 mixture of ethylenecarbonate/dimethylcarbonate). For comparison, also the pure Sn NCs and Ge NPs were tested. We note that there is a thin amorphous oxide layer on the surface of Sn NCs[29] formed upon exposure to air. Same thickness of oxide is also found on the Sn side of Sn−Ge NRs (Figure 1). Because as-synthesized NCs are capped with long-chain organic ligands (oleate and OLA), two kinds of surface modifications were tested in order to enable efficient electronic transport. The first approach is the ligand exchange with potassium hydrosulfide, as described in our recent report for Sn NCs.[29] The second strategy is the complete ligand removal *via* repetitive treatment with 1 M solution of hydrazine in acetonitrile, which is a method commonly used for quantum dot nanocrystal solids.[55]

The first discharge and charge capacities of the electrodes formulated as SnGe(30%)/CB(45%)/CMC-(25%) were 2400 and 1750 mAh g^{-1}, respectively, giving Coulombic efficiency (CE) of 73%. The irreversible capacity of 650 mAh g^{-1} is attributed to the formation

of an SEI layer. CE efficiencies in the subsequent cycles were above 99%. The average capacities during the first 100 cycles (Figure 3) were C^{film} = 456 mAh g^{-1}, C^{max}_{SnGe} = 1520 mAh g^{-1}, C^{min}_{SnGe} = 1220 mAh g^{-1}. Theoretical capacity for Sn−Ge NRs containing idential mass fractions of Sn and Ge would be (990 + 1624)/2 = 1307 mAh g^{-1}, assuming full lithiation of Sn and Ge to $Li_{22}Sn_5$ and $Li_{22}Ge_5$. Given that there are batch to batch variations of the Sn and Ge contents, along with irreversible capacities due to reduction of oxides, and other uncertainties, we can conclude that Sn−Ge NRs exhibit capacities close to theoretical at the 30% mass fraction of an active material in the electrode film. For comparison, we plot the best achievable capacities for Sn NCs obtained with identical formulation and electrochemical testing conditions. Shown in Figure 3 are the data for 10 nm Sn NCs, previously demonstrated to outperform 20 nm Sn NCs and commercial Sn and SnO_2 nanopowders.[29] The average values for the first 100 cycles are by a factor of 1.5−2 lower than for Sn−Ge NRs: C^{film} = 308 mAh g^{-1}, C^{max}_{Sn} = 924 mAh g^{-1}, C^{min}_{Sn} = 624 mAh g^{-1}. Furthermore, much higher first-cycle irreversible capacities of ~1800 mAh g^{-1} were obtained, corresponding to CE of just 40%.

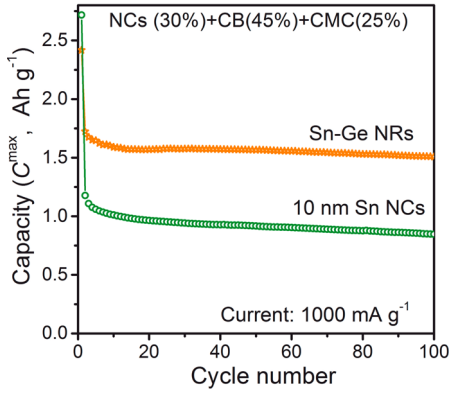

Figure 3. Reversible discharge capacities for anodes containing 30 wt % of Sn−Ge NRs and, for comparison, 30 wt % of Sn NCs. All NCs were ligand-exchanged with KHS prior to the preparation of the electrodes.

In order to increase an overall charge storage capacity of the electrode film (C^{film}), we increased the content of Sn−Ge NRs to ~64% (Figure 4). The first discharge and charge capacities are equal to 2100 and 1100 mAh/g, giving CE ~52%. The corresponding charge storage capacities are C^{film} = 633 mAh g^{-1}, C^{max}_{SnGe} = 990 mAh g^{-1}, C^{min}_{SnGe} = 924 mAh g^{-1}. These values are again by a factor of 1.5−2 higher than characteristics obtained for 10 nm Sn NCs (Figure 4A). Apparently, despite the notable increase of the overall electrode capacity (C^{film}) by ~40% due to the higher content of an active material, both Sn−Ge NRs and Sn NCs exhibit decrease of their fractional charge storage capacity (C^{min}) by ~25% for SnGe NRs and by ~10% for Sn NCs. Two different surface chemistries, ligand removal with N_2H_4 and ligand exchange with KHS, yielded electrodes with very similar capacities, but with slightly higher cycling stability for ligand-free material. We should also note that small and polydisperse Ge NPs (Figure S3) synthesized in the absence of Sn seeds, show much lower charge storage capacities (≤600 mAh g^{-1}, Figure S12) than Sn−Ge NRs studied under identical conditions. This is contrary to the recent report by Klavetter *et al.*,[10] who reported stable cycling for 70−120 nm Ge nanoparticles with reversible capacities above 1000 mAh g^{-1} under testing conditions similar to ours. As a plausible explanation, very small and polydisperse Ge particles may form a highly unstable SEI layer due to large specific surface area and may also contain excessive amount of oxides, further lowering the accessible reversible capacity.

One of the key advantages of nanoscopic particles is faster reaction kinetics due to short diffusion lengths, which can improve the retention of the capacity at high charge/discharge current densities. The characteristic time constant for diffusion is given by $t = L^2/D$, where L is the diffusion length and D is the diffusion coefficient. Short diffusion lengths and high Li diffusion coefficient in Ge[22,53] have led to high rate capabilities reported for Ge nanostructures, including hollow nanotubes[16] and nanoparticle-based slurries.[10] In accord with this expectation, SnGe NRs can retain up to

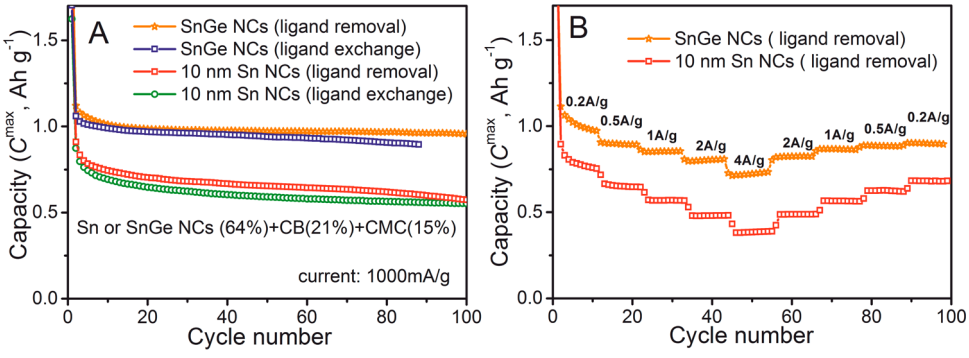

Figure 4. (A) Reversible discharge capacities for anodes comprising 15 × 25 nm SnGe NRs and, for comparison, 10 nm Sn NCs. (B) Rate-capability tests for 15 × 25 nm SnGe NRs and for 10 nm Sn NCs. All electrodes contained 64 wt % of an active material.

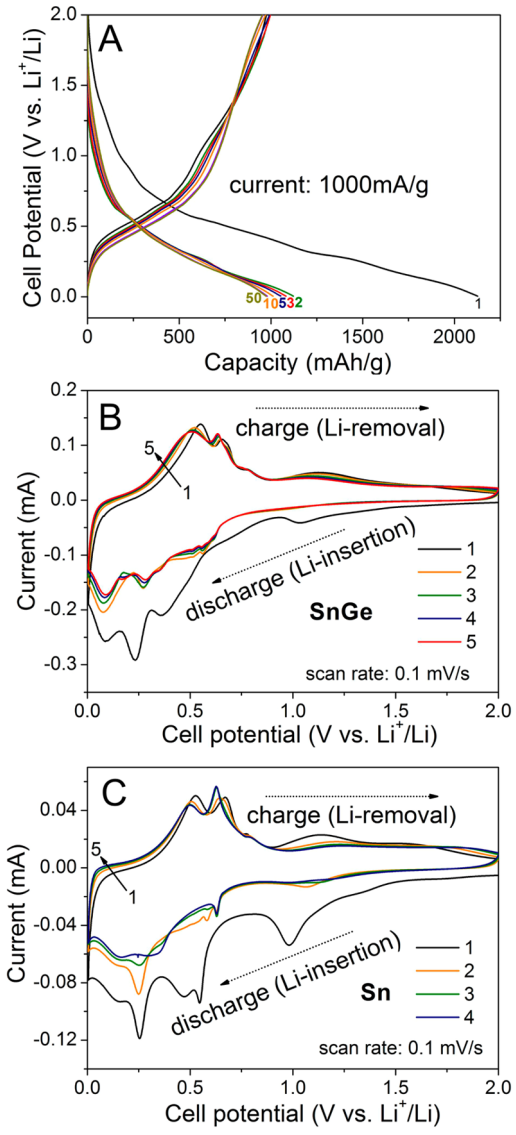

Figure 5. (A) Galvanostatic voltage discharge profiles for Sn−Ge NRs (f_{AM} = 0.64), corresponding to Figure 4A. (B,C) Cyclic voltammograms for the first five cycles for electrodes containing SnGe NRs and Sn NPs.

70−80% of the initial capacity when cycled at the high currents of ~4 A g^{-1} (Figure 4B). On the contrary, Sn NCs exhibit much faster decrease of capacity with increasing the current density to 4 A g^{-1} and lose at least 50% of their initial capacity. Furthermore, we tested nanoparticulate Si (≤50 nm, obtained from MTI corporation) using same electrode formulation and observed similar decrease of capacity by a factor of 2−3 upon increase of the current rate to 3−6 A g^{-1} (Figure S13). Also, the cycling stability of Sn−Ge NRs is considerably higher than for Sn (Figure 4A) and Si electrodes (Figure S13). The only apparent advantage of Si is its higher initial charge storage capacity of ~3 A g^{-1}. We note that our results for nanoparticulate Si are fully consistent with recent reports by others,[23,50,51,53,56] where Si NPs were also mixed with CB additive and CMC binder at similar weight proportions (60−65 wt % of Si).

Galvanostatic voltage profiles (Figure 5A) show that all Li-insertion and deinsertion processes are spread over relatively broad voltage range and, therefore, are also separated temporally. Closer insights are provided by the cycling votammograms (CVs, Figure 5B,C). The first-cycle CV contains multiple reduction waves starting above 1 V, corresponding to the formation of SEI layer and reduction of oxides (SnO, SnO_2, GeO_2), and these processes are irreversible. A cascade of reduction waves below 1 V (Li-insertion) is related to the formation of multiple Li−Sn alloys ($Li_{0.4}Sn$, $Li_{0.714}Sn$, $Li_{2.33}Sn$, $Li_{2.6}Sn$, $Li_{3.5}Sn$, $Li_{4.4}Sn$) and Li−Ge alloys (Li_9Ge_4, Li_7Ge_2, and $Li_{15}Ge_4$).[16,21,57] Cyclic voltammograms are also fully consistent with the earlier reports for nano- and microgranular SnO_2[57,58] and Sn,[59,60] Ge nanorods, and Ge nanowires.[10,27,38] Two peaks at 0.5 and 0.6 V in the positive (oxidation) current range correspond to all dealloying steps. Comparison with the CV curves of reference 15 nm Sn NPs (Figure 5C) and amorphous Ge NPs (Figure S12) shows that Sn and Ge retain their distinct electrochemical features also in Sn−Ge NR anodes. For instance, dealloying of Ge is usually seen as a broad feature centered at around +0.4 V (Figure S12) and delithiation of 15 nm Sn NPs appears to be stepwise with at least two peaks (Figure 5C), and these features are also present in CV curves of Sn−Ge NRs. We assume that temporally separated, stepwise lithiation and delithiation of Sn and Ge may help to decrease the mechanical stress during electrochemical cycling.

CONCLUSIONS

In summary, we demonstrated a simple colloidal synthesis of Sn−Ge NRs using Sn NPs as low-melting-point catalyst for the SLS growth. For two nearly immiscible materials such as Sn and Ge, preparation of Sn−Ge NRs can serve as ultimately the most optimal way to mix both components at the nanoscale and maintain characteristic grain sizes without applying energy-intense mechanical mixing. We showed that there is a synergistic effect of both components onto the Li-ion storage properties of the entire nanocomposite. Namely, Sn−Ge NRs exhibit charge storage capacities above 1000 mAh g^{-1}, by a factor 1.5−2 higher than capacities obtained with highly monodisperse Sn NPs under the same testing conditions and comparable to the best reports for Ge nanostructures.[10] Furthermore, Sn−Ge NRs show excellent rate capability, retaining 80% of the initial capacity after the increase of current density to 4 A g^{-1}. Insertion and removal of Li-ion is temporally separated in Sn and Ge, which may explain the improved cycling stability of Sn−Ge NRs. Future work should focus on

such well-defined nanocomposites of active materials as a general strategy for combining and enhancing their individual Li-ion (and also Na-ion) storage characteristics.

METHODS

Synthesis of Sn NPs (Crude Solution of Sn Seeds). In a typical synthesis of 15 nm Sn NPs, 10 g of OLA (70%, Sigma-Aldrich), dried at 105 °C under vacuum for 1 h, was heated to 180 °C under argon, followed by the consecutive injections of $LiN(SiMe_3)_2$ (1.8 mmol, 1.8 mL of 1 M solution in toluene, Sigma-Aldrich), $Sn[N(SiMe_3)_2]_2$ (Sigma-Aldrich, 0.25 mmol in 0.5 mL of squalane), and diisobutylaluminium hydride (0.35 mL of 1 M solution in toluene, Sigma-Aldrich), with 10 s delays between injections. In 45 min, the reaction solution was cooled to 70 °C with water bath and was used for synthesis of Sn−Ge NRs without further purification.

Synthesis of 15 × 25 nm Sn−Ge NRs Using a Crude Solution of Sn NPs. Ten grams of OLA, dried under vacuum at 105 °C under vacuum for 1 h, was heated to 300 °C, followed by the injection of a mixture containing $Ge[N(SiMe_3)_2]_2$ (100 μL, 0.25 mmol, 95%, ABCR), 0.35 mL of squalane, and 5 mL of Sn NC crude solution. After injection, the temperature dropped to ∼260 °C. In 2.5 min, the reaction mixture was quickly cooled to room temperature. When temperature reached 60 °C, 0.4 mL of oleic acid was added to improve colloidal stability through the displacement of weakly bound OLA molecules. Sn−Ge NRs were precipitated by adding toluene (∼5 mL) and ethanol (∼25 mL), separated by centrifugation, and redispersed in chloroform (∼5 mL) containing oleic acid (1%). The second precipitation was induced by adding ethanol, and after being centrifuged, Sn−Ge NRs were redispersed in chloroform (2 mL) and stored under ambient conditions. A typical reaction yield is ∼10 mg of Sn−Ge NRs.

One-Pot Synthesis of 15 × 25 nm Sn−Ge NRs. Ten grams of OLA, dried under vacuum at 105 °C for 1 h, was heated to 270 °C. During heating, several injections were performed. At 180 °C, $LiN(SiMe_3)_2$ (1.8 mmol, 1.8 mL of 1 M solution in toluene), then $Sn[N(SiMe_3)_2]_2$ 0.25 mmol in 0.5 mL squalane), and DIBAH (0.35 mL of 1 M solution in toluene) were injected with 10 s delays between injections. This leads to the instant formation of Sn NP seeds. At 230 °C, pure $Ge[N(SiMe_3)_2]_2$ (0.5 mmol, 200 μL) was injected. When temperature reached 270 °C (in 9−10 min after first injection), reaction was stopped by cooling to room temperature. The isolation and purification of Sn−Ge NRs was carried out identically to the procedure described in the previous paragraph.

Characterization. TEM images were recorded using a JEOL JEM-2200FS microscope operated at 200 kV, whereas STEM images were collected on Hitachi HD-2700 microscope operated at 200 kV. Powder XRD patterns were collected with STOE STADIP powder diffractometer. The Rietveld refinement of patterns was carried out using the program FULLPROF in the full pattern matching mode with the WinPLOTR interface. ATR-FTIR spectra were recorded using Thermo Scientific Nicolet iS5 FTIR spectrometer. Raman spectra were obtained using Thermoscientific DXR Raman microscope (455 nm laser for excitation).

Assembly and Testing of Li-Ion Halfcells. In a typical electrode preparation, CB (Super-P C65, TIMCAL), CMC binder (Daicel Fine Chem. Ltd.), and Sn−Ge NRs (or Sn and Si NPs) were combined into an aqueous slurry and ball-milled for 1 h before casting onto Ti current collector. All electrochemical measurements were conducted in a homemade, reusable, and airtight coin-type cells, assembled in an argon-filled glovebox with water and oxygen levels below 1 ppm. Lithium metal served as both reference and counter electrode. Working electrode was covered with Celgard separator membrane, and a glass fiber separator of 1 mm thickness was placed between working and reference electrode. A 1 M solution of $LiPF_6$ in ethylene-carbonate/dimethylcarbonate mixture (1:1 w/w, containing 3% of FEC) was used as an electrolyte. All charge−discharge galvanostatic tests and cyclic voltammetry scans were obtained with MPG2 multichannel workstation (Bio Logic).

Conflict of Interest: The authors declare no competing financial interest.

Acknowledgment. M.I.B. thanks the Swiss National Science Foundation for the Marie Heim Vögtlin grant. M.V.K. acknowledges financial support from the Swiss National Science Foundation (SNF-Project Nr. 200021_140245) and Swiss Federal Commission for Technology and Innovation (CTI-Projekt Nr. 14698.2 PFIW-IW). We thank Prof. Christoph Müller and Imtiaz Qasim (ETH Zürich) for a help with Raman measurements. Electron microscopy was performed at ETH Zürich Electron Microscopy Center and at Empa Electron Microscopy Center.

Supporting Information Available: Additional figures are provided in the Supporting Information. This material is available free of charge *via* the Internet at http://pubs.acs.org.

REFERENCES AND NOTES

1. Talapin, D. V.; Lee, J.-S.; Kovalenko, M. V.; Shevchenko, E. V. Prospects of Colloidal Nanocrystals for Electronic and Optoelectronic Applications. *Chem. Rev.* **2010**, *110*, 389–458.
2. Park, J.; An, K. J.; Hwang, Y. S.; Park, J. G.; Noh, H. J.; Kim, J. Y.; Park, J. H.; Hwang, N. M.; Hyeon, T. Ultra-Large-Scale Syntheses of Monodisperse Nanocrystals. *Nat. Mater.* **2004**, *3*, 891–895.
3. Galland, C.; Ghosh, Y.; Steinbrück, A.; Hollingsworth, J. A.; Htoon, H.; Klimov, V. I. Lifetime Blinking in Nonblinking Nanocrystal Quantum Dots. *Nat. Commun.* **2012**, *3*, 908.
4. Law, M.; Luther, J. M.; Song, Q.; Hughes, B. K.; Perkins, C. L.; Nozik, A. J. Structural, Optical, and Electrical Properties of PbSe Nanocrystal Solids Treated Thermally or with Simple Amines. *J. Am. Chem. Soc.* **2008**, *130*, 5974–5985.
5. McDonald, S. A.; Konstantatos, G.; Zhang, S. G.; Cyr, P. W.; Klem, E. J. D.; Levina, L.; Sargent, E. H. Solution-Processed PbS Quantum Dot Infrared Photodetectors and Photovoltaics. *Nat. Mater.* **2005**, *4*, 138–142.
6. Urban, J. J.; Talapin, D. V.; Shevchenko, E. V.; Kagan, C. R.; Murray, C. B. Synergism in Binary Nanocrystal Superlattices Leads to Enhanced p-Type Conductivity in Self-Assembled PbTe/Ag_2Te Thin Films. *Nat. Mater.* **2007**, *6*, 115–121.
7. Guyot-Sionnest, P. Electrical Transport in Colloidal Quantum Dot Films. *J. Phys. Chem. Lett.* **2012**, *3*, 1169–1175.
8. Dang, C.; Lee, J.; Breen, C.; Steckel, J. S.; Coe-Sullivan, S.; Nurmikko, A. Red, Green and Blue Lasing Enabled by Single-Exciton Gain in Colloidal Quantum Dot Films. *Nat. Nanotechnol.* **2012**, *7*, 335–339.
9. Xu, L. P.; Kim, C.; Shukla, A. K.; Dong, A. G.; Mattox, T. M.; Milliron, D. J.; Cabana, J. Monodisperse Sn Nanocrystals as a Platform for the Study of Mechanical Damage during Electrochemical Reactions with Li. *Nano Lett.* **2013**, *13*, 1800–1805.
10. Kim, M. G.; Cho, J. Nanocomposite of Amorphous Ge and Sn Nanoparticles as an Anode Material for Li Secondary Battery. *J. Electrochem. Soc.* **2009**, *156*, A277–A282.
11. Gibot, P.; Casas-Cabanas, M.; Laffont, L.; Levasseur, S.; Carlach, P.; Hamelet, S.; Tarascon, J. M.; Masquelier, C. Room-Temperature Single-Phase Li Insertion/Extraction in Nanoscale Li_xFePO_4. *Nat. Mater.* **2008**, *7*, 741–747.
12. Wang, X. L.; Feygenson, M.; Chen, H. Y.; Lin, C. H.; Ku, W.; Bai, J. M.; Aronson, M. C.; Tyson, T. A.; Han, W. Q. Nanospheres of a New Intermetallic $FeSn_5$ Phase: Synthesis, Magnetic Properties and Anode Performance in Li-Ion Batteries. *J. Am. Chem. Soc.* **2011**, *133*, 11213–11219.
13. Oh, M. H.; Yu, T.; Yu, S. H.; Lim, B.; Ko, K. T.; Willinger, M. G.; Seo, D. H.; Kim, B. H.; Cho, M. G.; Park, J. H.; *et al.* Galvanic Replacement Reactions in Metal Oxide Nanocrystals. *Science* **2013**, *340*, 964–968.

14. Jang, B.; Park, M.; Chae, O. B.; Park, S.; Kim, Y.; Oh, S. M.; Piao, Y.; Hyeon, T. Direct Synthesis of Self-Assembled Ferrite/Carbon Hybrid Nanosheets for High Performance Lithium-Ion Battery Anodes. *J. Am. Chem. Soc.* **2012**, *134*, 15010–15015.
15. Choi, D. W.; Wang, D. H.; Bae, I. T.; Xiao, J.; Nie, Z. M.; Wang, W.; Viswanathan, V. V.; Lee, Y. J.; Zhang, J. G.; Graff, G. L.; *et al.* $LiMnPO_4$ Nanoplate Grown *via* Solid-State Reaction in Molten Hydrocarbon for Li-Ion Battery Cathode. *Nano Lett.* **2010**, *10*, 2799–2805.
16. Yoon, S.; Park, C.-M.; Sohn, H.-J. Electrochemical Characterizations of Germanium and Carbon-Coated Germanium Composite Anode for Lithium-Ion Batteries. *Electrochem. Solid State* **2008**, *11*, A42–A45.
17. Palacin, M. R. Recent Advances in Rechargeable Battery Materials: A Chemist's Perspective. *Chem. Soc. Rev.* **2009**, *38*, 2565–2575.
18. Goodenough, J. B.; Kim, Y. Challenges for Rechargeable Li Batteries. *Chem. Mater.* **2009**, *22*, 587–603.
19. Larcher, D.; Beattie, S.; Morcrette, M.; Edstrom, K.; Jumas, J.-C.; Tarascon, J.-M. Recent Findings and Prospects in the Field of Pure Metals as Negative Electrodes for Li-Ion Batteries. *J. Mater. Chem.* **2007**, *17*, 3759–3772.
20. Hayner, C. M.; Zhao, X.; Kung, H. H. Materials for Rechargeable Lithium-Ion Batteries. *Annu. Rev. Chem. Biomol. Eng.* **2012**, *3*, 445–471.
21. Baggetto, L.; Notten, P. H. L. Lithium-Ion (De)Insertion Reaction of Germanium Thin-Film Electrodes: An Electrochemical and *In Situ* XRD Study. *J. Electrochem. Soc.* **2009**, *156*, A169–A175.
22. Fuller, C. S.; Severiens, J. C. Mobility of Impurity Ions in Germanium and Silicon. *Phys. Rev.* **1954**, *96*, 21–24.
23. Kovalenko, I.; Zdyrko, B.; Magasinski, A.; Hertzberg, B.; Milicev, Z.; Burtovyy, R.; Luzinov, I.; Yushin, G. A Major Constituent of Brown Algae for Use in High-Capacity Li-Ion Batteries. *Science* **2011**, *333*, 75–79.
24. Chan, C. K.; Peng, H.; Liu, G.; McIlwrath, K.; Zhang, X. F.; Huggins, R. A.; Cui, Y. High-Performance Lithium Battery Anodes Using Silicon Nanowires. *Nat. Nanotechnol.* **2008**, *3*, 31–35.
25. Magasinski, A.; Dixon, P.; Hertzberg, B.; Kvit, A.; Ayala, J.; Yushin, G. High-Performance Lithium-Ion Anodes Using a Hierarchical Bottom-Up Approach. *Nat. Mater.* **2010**, *9*, 353–358.
26. Chockla, A. M.; Klavetter, K. C.; Mullins, C. B.; Korgel, B. A. Tin-Seeded Silicon Nanowires for High Capacity Li-Ion Batteries. *Chem. Mater.* **2012**, *24*, 3738–3745.
27. Chockla, A. M.; Klavetter, K. C.; Mullins, C. B.; Korgel, B. A. Solution-Grown Germanium Nanowire Anodes for Lithium-Ion Batteries. *ACS Appl. Mater. Interfaces* **2012**, *4*, 4658–4664.
28. Beattie, S. D.; Larcher, D.; Morcrette, M.; Simon, B.; Tarascon, J. M. Si Electrodes for Li-ion Batteries—A New Way To Look at an Old Problem. *J. Electrochem. Soc.* **2008**, *155*, 158–163.
29. Kravchyk, K.; Protesescu, L.; Bodnarchuk, M. I.; Krumeich, F.; Yarema, M.; Walter, M.; Guntlin, C.; Kovalenko, M. V. Monodisperse and Inorganically Capped Sn and Sn/SnO_2 Nanocrystals for High-Performance Li-Ion Battery Anodes. *J. Am. Chem. Soc.* **2013**, *135*, 4199–4202.
30. Cho, Y. J.; Kim, C. H.; Im, H. S.; Myung, Y.; Kim, H. S.; Back, S. H.; Lim, Y. R.; Jung, C. S.; Jang, D. M.; Park, J.; *et al.* Germanium–Tin Alloy Nanocrystals for High-Performance Lithium Ion Batteries. *Phys. Chem. Chem. Phys.* **2013**, *15*, 11691–11695.
31. Lee, H.; Cho, J. $Sn_{78}Ge_{22}$@Carbon Core–Shell Nanowires as Fast and High-Capacity Lithium Storage Media. *Nano Lett.* **2007**, *7*, 2638–2641.
32. Chevalier, P. Y. A Thermodynamic Evaluation of the Au–Ge and Au–Si Systems. *Thermochim. Acta* **1989**, *141*, 217–226.
33. Trentler, T. J.; Hickman, K. M.; Goel, S. C.; Viano, A. M.; Gibbons, P. C.; Buhro, W. E. Solution–Liquid–Solid Growth Of Crystalline III–V Semiconductors: An Analogy to Vapor–Liquid–Solid Growth. *Science* **1995**, *270*, 1791–1794.
34. Wang, F. D.; Dong, A. G.; Sun, J. W.; Tang, R.; Yu, H.; Buhro, W. E. Solution–Liquid–Solid Growth of Semiconductor Nanowires. *Inorg. Chem.* **2006**, *45*, 7511–7521.
35. Yu, H.; Li, J. B.; Loomis, R. A.; Gibbons, P. C.; Wang, L. W.; Buhro, W. E. Cadmium Selenide Quantum Wires and the Transition from 3D to 2D Confinement. *J. Am. Chem. Soc.* **2003**, *125*, 16168–16169.
36. Olesinski, R. W.; Abbaschian, G. J. The Si–Sn (Silicon–Tin) System. *Bull. Alloy Phase Diagrams* **1984**, *5*, 273–276.
37. Lu, X.; Hessel, C. M.; Yu, Y.; Bogart, T. D.; Korgel, B. A. Colloidal Luminescent Silicon Nanorods. *Nano Lett.* **2013**, *13*, 3101–3105.
38. Chockla, A. M.; Harris, J. T.; Korgel, B. A. Colloidal Synthesis of Germanium Nanorods. *Chem. Mater.* **2011**, *23*, 1964–1970.
39. Lee, D. C.; Pietryga, J. M.; Robel, I.; Werder, D. J.; Schaller, R. D.; Klimov, V. I. Colloidal Synthesis of Infrared-Emitting Germanium Nanocrystals. *J. Am. Chem. Soc.* **2009**, *131*, 3436–3437.
40. Chockla, A. M.; Bogart, T. D.; Hessel, C. M.; Klavetter, K. C.; Mullins, C. B.; Korgel, B. A. Influences of Gold, Binder and Electrolyte on Silicon Nanowire Performance in Li-Ion Batteries. *J. Phys. Chem. C* **2012**, *116*, 18079–18086.
41. Vaughn, D. D., II; Schaak, R. E. Synthesis, Properties and Applications of Colloidal Germanium and Germanium-Based Nanomaterials. *Chem. Soc. Rev.* **2013**, *42*, 2861–2879.
42. Muthuswamy, E.; Iskandar, A. S.; Amador, M. M.; Kauzlarich, S. M. Facile Synthesis of Germanium Nanoparticles with Size Control: Microwave *versus* Conventional Heating. *Chem. Mater.* **2012**, *25*, 1416–1422.
43. Ruddy, D. A.; Johnson, J. C.; Smith, E. R.; Neale, N. R. Size and Bandgap Control in the Solution-Phase Synthesis of Near-Infrared-Emitting Germanium Nanocrystals. *ACS Nano* **2010**, *4*, 7459–7466.
44. Gerung, H.; Bunge, S. D.; Boyle, T. J.; Brinker, C. J.; Han, S. M. Anhydrous Solution Synthesis of Germanium Nanocrystals from the Germanium(II) Precursor $Ge[N(SiMe_3)_2]_2$. *Chem. Commun.* **2005**, 1914–1916.
45. Read, C. G.; Biacchi, A. J.; Schaak, R. E. Au–Ge and Ag–Ge Heterodimers with Tunable Domain Sizes: A Supersaturation-Precipitation Route to Colloidal Hybrid Nanoparticles. *Chem. Mater.* **2013**, *25*, 4304–4311.
46. Ihm, J.; Cohen, M. L. Equilibrium Properties and the Phase Transition of Grey and White Tin. *Phys. Rev. B* **1981**, *23*, 1576–1579.
47. Fan, S.; Lim, L. L.; Tay, Y. Y.; Pramana, S.; Rui, X.; Samani, M. K.; Yan, Q.; Tay, B. K.; Toney, M. F.; Hng, H. H. Rapid Fabrication of Novel Sn–Ge Alloy: Structure–Property Relationship and Its Enhanced Lithium Storage Properties. *J. Mater. Chem. A.* **2013**, *1*, 14577–14585.
48. Cheng, R.; Wang, W.; Gong, X.; Sun, L.; Guo, P.; Hu, H.; Shen, Z.; Han, G.; Yeo, Y.-C. Relaxed and Strained Patterned Germanium-Tin Structures: A Raman Scattering Study. *ECS J. Solid State Sci. Technol.* **2013**, *2*, P138–P145.
49. Su, S.; Wang, W.; Cheng, B.; Hu, W.; Zhang, G.; Xue, C.; Zuo, Y.; Wang, Q. The Contributions of Composition and Strain to the Phonon Shift in Alloys. *Solid State Commun.* **2011**, *151*, 647–650.
50. Erk, C.; Brezesinski, T.; Sommer, H.; Schneider, R.; Janek, J. Toward Silicon Anodes for Next-Generation Lithium Ion Batteries: A Comparative Performance Study of Various Polymer Binders and Silicon Nanopowders. *ACS Appl. Mater. Interfaces* **2013**, *5*, 7299–7307.
51. Magasinski, A.; Zdyrko, B.; Kovalenko, I.; Hertzberg, B.; Burtovyy, R.; Huebner, C. F.; Fuller, T. F.; Luzinov, I.; Yushin, G. Toward Efficient Binders for Li-Ion Battery Si-Based Anodes: Polyacrylic Acid. *ACS Appl. Mater. Interfaces* **2010**, *2*, 3004–3010.
52. Xiao, J.; Xu, W.; Wang, D.; Choi, D.; Wang, W.; Li, X.; Graff, G. L.; Liu, J.; Zhang, J.-G. Stabilization of Silicon Anode for Li-Ion Batteries. *J. Electrochem. Soc.* **2010**, *157*, A1047–A1051.
53. Bridel, J. S.; Azaïs, T.; Morcrette, M.; Tarascon, J. M.; Larcher, D. Key Parameters Governing the Reversibility of

Si/Carbon/CMC Electrodes for Li-Ion Batteries. *Chem. Mater.* **2009**, *22*, 1229–1241.
54. Mazouzi, D.; Lestriez, B.; Roué, L.; Guyomard, D. Silicon Composite Electrode with High Capacity and Long Cycle Life. *Electrochem. Solid State* **2009**, *12*, A215–A218.
55. Talapin, D. V.; Murray, C. B. PbSe Nanocrystal Solids for n- and p-Channel Thin Film Field-Effect Transistors. *Science* **2005**, *310*, 86–89.
56. Koo, B.; Kim, H.; Cho, Y.; Lee, K. T.; Choi, N.-S.; Cho, J. A Highly Cross-Linked Polymeric Binder for High-Performance Silicon Negative Electrodes in Lithium Ion Batteries. *Angew. Chem., Int. Ed.* **2012**, *51*, 8762–8767.
57. Courtney, I. A.; Dahn, J. R. Electrochemical and *In Situ* X-ray Diffraction Studies of the Reaction of Lithium with Tin Oxide Composites. *J. Electrochem. Soc.* **1997**, *144*, 2045–2052.
58. Park, M.-S.; Wang, G.-X.; Kang, Y.-M.; Wexler, D.; Dou, S.-X.; Liu, H.-K. Preparation and Electrochemical Properties of SnO_2 Nanowires for Application in Lithium-Ion Batteries. *Angew. Chem., Int. Ed.* **2007**, *46*, 750–753.
59. Li, N. C.; Martin, C. R. A High-Rate, High-Capacity, Nanostructured Sn-Based Anode Prepared Using Sol−Gel Template Synthesis. *J. Electrochem. Soc.* **2001**, *148*, A164–A170.
60. Yu, Y.; Gu, L.; Wang, C.; Dhanabalan, A.; van Aken, P. A.; Maier, J. Encapsulation of Sn@Carbon Nanoparticles in Bamboo-like Hollow Carbon Nanofibers as an Anode Material in Lithium-Based Batteries. *Angew. Chem., Int. Ed.* **2009**, *48*, 6485–6489.